

Prospects for probing light photophobic axion-like particles via displaced vertex signals at the CEPC

Chong-Xing Yue^{1,2*} and Xin-Yang Li^{1,2†}

¹*Department of Physics, Liaoning Normal University, Dalian 116029, China*

²*Center for Theoretical and Experimental High Energy Physics,
Liaoning Normal University, Dalian 116029, China*

Abstract

In recent years, long-lived particles (LLPs) have attracted increasing attention in searches for physics beyond the Standard Model (SM). In this paper, we investigate the discovery prospects for light long-lived ALPs predicted by the photophobic ALP scenario via displaced vertex signals at the CEPC with the center-of-mass energy $\sqrt{s} = 91.2$ GeV and integrated luminosity $\mathcal{L} = 100$ ab⁻¹. After comparing several possible single-production processes of the photophobic ALP, we focus on the dominant process $e^+e^- \rightarrow Z \rightarrow a\gamma$, with the ALP a subsequently decaying into a pair of displaced charged leptons. Dedicated Monte Carlo simulations are performed for the $\mu^+\mu^-\gamma$ and $\tau_h^+\tau_h^-\cancel{E}_T\gamma$ signals. For the $\mu^+\mu^-\gamma$ signal, the CEPC is sensitive to the parameter region $g_{aWW} \in [1.27 \times 10^{-3}, 6.80 \times 10^{-1}]$ TeV⁻¹ for $m_a \in [1, 4]$ GeV. For the $\tau_h^+\tau_h^-\cancel{E}_T\gamma$ signal, the accessible region is $g_{aWW} \in [7.00 \times 10^{-4}, 9.40 \times 10^{-3}]$ TeV⁻¹ with $m_a \in [4, 9]$ GeV. These results demonstrate the strong potential of the CEPC to explore light long-lived ALPs via displaced vertex signals, providing complementary coverage to existing searches at the LEP and LHC, as well as to the projected reach of the HL-LHC.

*cxyue@lnnu.edu.cn

†lxy91108@163.com (Corresponding author)

I. INTRODUCTION

The origin of neutrino masses [1], the nature of dark matter [2, 3], the strong CP problem [4–6] and the hierarchy problem [7] remain some of the deepest mysteries in particle physics. Over the past decades, many experimental efforts addressing these puzzles have focused on new particles with sizeable couplings to the Standard Model (SM) and masses above several hundred GeV or even at the TeV scale. More recently, lighter feebly interacting particles (FIPs) [8, 9] with masses at the GeV scale have emerged as a well-motivated and complementary possibility. Owing to their extremely weak interactions with the SM particles, these FIPs are typically long-lived and may decay at a macroscopic distance from their production point. When such decays occur within the detector, their visible decay products can be reconstructed as displaced vertices (DVs). Consequently, conventional searches targeting promptly decaying signals often lose sensitivity, whereas displaced vertex signals provide a promising avenue for detecting long-lived particles (LLPs) [10].

Searches for LLPs have been extensively pursued at the LHC. The ATLAS, CMS and LHCb Collaborations have conducted numerous analyses based on displaced vertex signals (see, e.g., Refs. [11–28]). While the LHC demonstrates strong sensitivity across a broad range of LLP scenarios, future lepton colliders such as the CEPC [29, 30] and FCC-ee [31, 32] can also offer a complementary and promising platform for LLP searches. Operating as Z -boson and Higgs-boson factories, these facilities are expected to produce up to 4.1×10^{12} Z bosons and 4.3×10^6 Higgs bosons [33], enabling unprecedented electroweak and Higgs precision measurements. Moreover, the clean experimental environment and high integrated luminosity of these colliders are expected to yield reduced backgrounds and enhanced sensitivity to LLPs. Motivated by these advantages, numerous studies [34–42] have been performed at future lepton colliders to explore the phenomenology of LLPs, such as vector-like leptons (VLLs) and axion-like particles (ALPs).

ALPs [43–48] are one of the most well-motivated candidates for feebly interacting particles. They are pseudo-Nambu-Goldstone bosons associated with the spontaneous breaking of global $U(1)$ symmetries and appear as singlet pseudoscalars under the SM gauge groups. Over the years, a wide range of new physics scenarios have predicted the existence of ALPs. Of particular interest is the photophobic ALP scenario [49], where the ALP has no tree-level couplings to the SM photons or fermions and interacts only with other electroweak gauge bosons (WW , ZZ , $Z\gamma$)

at tree level. Although direct couplings to photons and fermions are absent, the interactions of ALP with electroweak gauge bosons can induce effective ALP-fermion and ALP-photon couplings at loop level. Most existing phenomenological studies have focused on exploring heavy photophobic ALPs and their prompt-decay signals [50–54]. However, the ALPs predicted by this scenario can be long-lived, particularly in the low-mass region. When the photophobic ALP mass lies below the threshold for on-shell decays into massive electroweak gauge bosons, these channels are kinematically forbidden. The light photophobic ALPs then decay predominantly through loop-induced channels into fermions and photons, leading to a suppressed total width and an enhanced proper decay length. As a result, light photophobic ALPs can manifest as LLPs, giving rise to distinctive signals at high-energy colliders. Motivated by this feature, several studies have explored the phenomenology of long-lived photophobic ALPs. For instance, Ref. [55] has investigated prompt-lepton and mono-photon signals of these ALPs at future lepton colliders. However, when the ALP decay length becomes comparable to the detector scale, displaced vertex searches provide a powerful and complementary probe, accessing regions of parameter space that are not efficiently covered by prompt-decay and missing-energy searches. Future lepton colliders, such as the CEPC, offer a promising opportunity to probe light long-lived photophobic ALPs via displaced vertex signals, owing to their clean experimental environment, high integrated luminosity and precise measurement capabilities.

In this paper, we investigate the prospects for probing light long-lived photophobic ALPs via displaced vertex signals within the inner tracker detector (IT) of the CEPC with the center-of-mass energy $\sqrt{s} = 91.2$ GeV and integrated luminosity $\mathcal{L} = 100$ ab⁻¹. We consider the production of a photophobic ALP in association with a photon γ , a lepton pair or a jet pair. Among these production processes, the photon-associated production mode exhibits the largest production cross section. We therefore focus on the process $e^+e^- \rightarrow Z \rightarrow a\gamma$ as a representative example, where the ALP a subsequently decays into a pair of displaced charged leptons. Our analysis demonstrates that the CEPC can probe regions of parameter space that remain unexplored by current and future collider experiments, providing sensitivity complementary to previous searches.

The paper is organized as follows. In Sec. II, we introduce the theoretical framework of photophobic ALPs, discuss their possible decay modes and lifetimes, and analyze their single production at the CEPC. In Sec. III, we present a detailed analysis for the possibility of de-

tecting light long-lived photophobic ALPs via the process $e^+e^- \rightarrow Z \rightarrow a\gamma$, with the ALP a subsequently decaying into a pair of displaced charged leptons within the inner tracker detector of the CEPC. In Sec. IV, we summarize our conclusions and discussions.

II. THE THEORY FRAMEWORK

We consider the photophobic ALP scenario [49], in which the ALP interacts solely to the $SU(2)_L$ and $U(1)_Y$ gauge bosons, while tree-level couplings of ALP to fermions g_{aff} and gluons g_{aGG} are absent. This setup is consistent with the ultraviolet (UV) boundary conditions at the high scale Λ . The effective Lagrangian before the electroweak symmetry breaking can be written as [56]

$$\mathcal{L}_{\text{ALP}} = \frac{1}{2}\partial_\mu a \partial^\mu a - \frac{1}{2}m_a^2 a^2 - c_{\tilde{W}} \frac{a}{f_a} W_{\mu\nu}^i \tilde{W}^{\mu\nu,i} - c_{\tilde{B}} \frac{a}{f_a} B_{\mu\nu} \tilde{B}^{\mu\nu}, \quad (1)$$

where $W_{\mu\nu}^i$ and $B_{\mu\nu}$ respectively represent the gauge field strength tensors associated with the $SU(2)_L$ and $U(1)_Y$ gauge groups. The corresponding dual field strength tensors are defined as $\tilde{V}^{\mu\nu} = \frac{1}{2}\epsilon^{\mu\nu\lambda\kappa} V_{\lambda\kappa}$ ($V = W^i, B$), with $\epsilon^{0123} = 1$. The ALP mass and its decay constant are denoted by m_a and f_a , respectively. The coefficients $c_{\tilde{W}}/f_a$, $c_{\tilde{B}}/f_a$ and m_a are treated as independent free parameters.

After electroweak symmetry breaking, the interactions of ALP with the electroweak gauge bosons can be written as

$$\mathcal{L}_{\text{ALP}} = -\frac{1}{4}g_{a\gamma\gamma} a F_{\mu\nu} \tilde{F}^{\mu\nu} - \frac{1}{2}g_{a\gamma Z} a Z_{\mu\nu} \tilde{F}^{\mu\nu} - \frac{1}{4}g_{aZZ} a Z_{\mu\nu} \tilde{Z}^{\mu\nu} - \frac{1}{2}g_{aWW} a W_{\mu\nu}^+ \tilde{W}^{\mu\nu,-}, \quad (2)$$

where the corresponding coupling constants are defined as

$$\begin{aligned} g_{a\gamma\gamma} &= \frac{4}{f_a}(s_W^2 c_{\tilde{W}} + c_W^2 c_{\tilde{B}}), & g_{a\gamma Z} &= \frac{4}{f_a} s_W c_W (c_{\tilde{W}} - c_{\tilde{B}}), \\ g_{aZZ} &= \frac{4}{f_a}(c_W^2 c_{\tilde{W}} + s_W^2 c_{\tilde{B}}), & g_{aWW} &= \frac{4}{f_a} c_{\tilde{W}}, \end{aligned} \quad (3)$$

with s_W and c_W denoting the sine and cosine of the Weinberg angle, respectively. In the photophobic ALP scenario, the tree-level coupling of ALP to photons vanishes as a consequence of the UV boundary conditions (see Ref. [49] for details). Accordingly, $g_{a\gamma\gamma} = \frac{4}{f_a}(s_W^2 c_{\tilde{W}} + c_W^2 c_{\tilde{B}}) = 0$, which leads to the relation $s_W^2 c_{\tilde{W}} + c_W^2 c_{\tilde{B}} = 0$. Consequently, the couplings $g_{a\gamma Z}$, g_{aZZ} and g_{aWW} are not independent and can be expressed as

$$g_{aZ\gamma} = \frac{s_W}{c_W} g_{aWW}, \quad g_{aZZ} = \frac{c_{2W}}{c_W^2} g_{aWW}. \quad (4)$$

Therefore, the photophobic ALP scenario can be characterized by the ALP mass m_a and the coupling g_{aWW} .

Owing to the UV boundary conditions, tree-level ALP-fermion interactions vanish. However, the effective ALP-fermion coupling can be generated through one-loop renormalization group evolution (RGE) from the UV scale Λ down to the electroweak scale, which can be written as [57, 58]

$$\begin{aligned} g_{aff}^{\text{eff}} &= \frac{3}{4s_W^2} \frac{\alpha}{4\pi} g_{aWW} \ln \frac{\Lambda^2}{m_W^2} \\ &+ \frac{3}{c_W^2} \frac{\alpha}{4\pi} g_{aWW} Q_f (I_3^f - 2Q_f s_W^2) \ln \frac{\Lambda^2}{m_Z^2} \\ &+ \frac{3c_{2W}}{s_W^2 c_W^4} \frac{\alpha}{4\pi} g_{aWW} (Q_f^2 s_W^4 - I_3^f Q_f s_W^2 + \frac{1}{8}) \ln \frac{\Lambda^2}{m_Z^2}. \end{aligned} \quad (5)$$

Here Q_f and I_3^f denote the electric charge and the third component of weak isospin of the fermion f , respectively, and $\alpha = e^2/(4\pi)$ is the fine-structure constant. The cutoff scale is taken to be $4\pi f_a = 4\pi \times 10$ TeV in this paper. In the above expression, we keep only the terms containing $\ln(\Lambda^2/m_V^2)$ (with $V = Z, W$), which are logarithmically enhanced. The subleading terms are given in Refs. [57–59], but they are numerically small and can be safely neglected in our analysis.

The couplings of ALP to the electroweak gauge bosons can induce a small effective ALP-photon coupling at one loop [57], which can be expressed as

$$g_{a\gamma\gamma}^{\text{eff}} = \frac{2\alpha}{\pi} g_{aWW} B_2(\tau_W), \quad (6)$$

where the loop function B_2 is defined as

$$B_2(\tau) = 1 - (\tau - 1)f^2(\tau), \quad \text{with } f(\tau) = \begin{cases} \arcsin \frac{1}{\sqrt{\tau}}, & \text{for } \tau \geq 1 \\ \frac{\pi}{2} + \frac{i}{2} \log \frac{1+\sqrt{1-\tau}}{1-\sqrt{1-\tau}}, & \text{for } \tau < 1 \end{cases}, \quad (7)$$

with $\tau_W = 4m_W^2/m_a^2$.

Under the UV boundary conditions mentioned above, the ALP does not couple directly to gluons. However, the effective ALP-fermion coupling g_{aff}^{eff} can induce the effective ALP-gluon coupling at one loop. Since g_{aff}^{eff} itself arises from ALP interactions with electroweak gauge

bosons at one loop, the resulting ALP-gluon coupling appears at two-loop level, which can be written as [50]

$$g_{aGG}^{\text{eff}} = \frac{1}{32\pi^2} \sum_{f=u,d,s} g_{aff}^{\text{eff}}. \quad (8)$$

Since this coupling arises at least at two-loop level and is therefore highly suppressed, its contribution to the signal processes considered in this study is negligible and can be safely ignored.

As discussed above, the ALP can exhibit a variety of decay modes, depending on its mass and the corresponding kinematic thresholds. The specific branching ratios for different ALP decay modes are shown in Fig. 1. As shown in this figure, for relatively light ALPs, tree-level decays into massive electroweak gauge bosons are kinematically forbidden. In this mass range, these light ALPs decay predominantly via loop-induced channels into the fermions. More specifically, within the mass range $2m_\mu \leq m_a \leq 2m_c$, the dominant decay modes are $s\bar{s}$ and $\mu^+\mu^-$. When $2m_c \leq m_a \leq 2m_b$, the $c\bar{c}$ and $\tau^+\tau^-$ channels become dominant. For $m_a \geq 2m_b$, the $b\bar{b}$ channel becomes dominant, while $c\bar{c}$ and $\tau^+\tau^-$ remain subdominant.

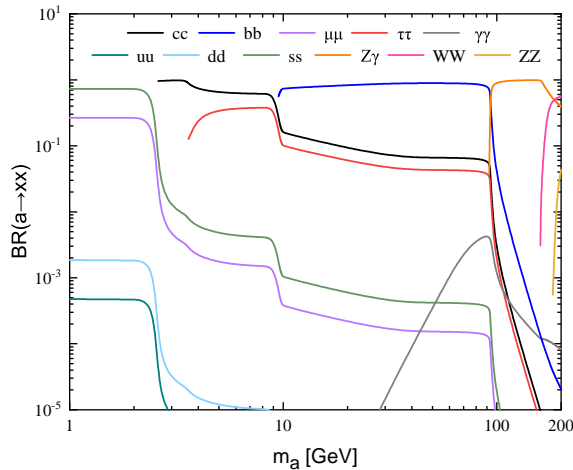


FIG. 1: The branching ratios of different photophobic ALP decay modes as functions of its mass m_a .

In this paper, we focus on the ALPs with masses in the range of 1 – 10 GeV and investigate their displaced vertex signals within the photophobic ALP scenario. In this mass range, the ALP predominantly decays into fermions via loop-induced couplings. These loop-induced

couplings suppress the total decay width, allowing the ALP to behave as a long-lived particle and propagate a measurable distance inside the detector before decaying. The decay length in the laboratory frame is given by

$$L_a = \beta_a \gamma_a c \tau_a = \frac{c |\vec{p}_a|}{m_a \Gamma_a}, \quad (9)$$

where $\Gamma_a = 1/\tau_a$ is the total decay width of the ALP, and β_a as well as γ_a denote its velocity and Lorentz boost factor, respectively. $\beta_a \gamma_a = |\vec{p}_a|/m_a$ with \vec{p}_a being the three-momentum of the ALP. The proper decay length $c\tau_a$ as a function of the ALP mass m_a for several representative values of the coupling g_{aWW} is shown in Figure 2. As illustrated in this figure, the $c\tau_a$ exhibits strong dependence on both m_a and g_{aWW} , increasing significantly as these parameters decrease. This wide range of proper decay lengths indicates that ALPs can be long-lived over a substantial region of parameter space. These long-lived ALPs can travel macroscopic distances before decaying within the detector, giving rise to distinctive DV signals that complement conventional ALP searches and can be efficiently explored within the IT of the CEPC.

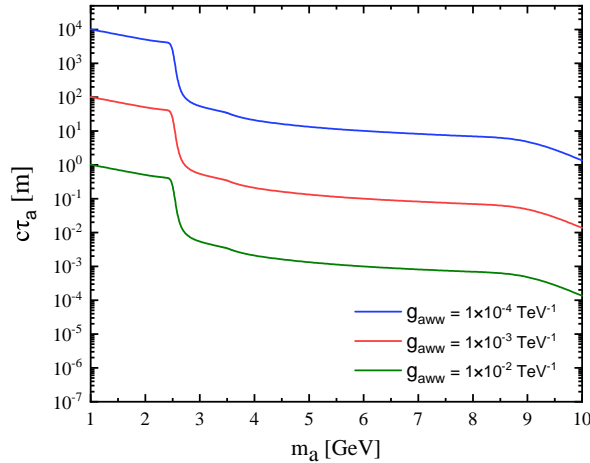


FIG. 2: The proper decay length of the ALP as functions of its mass m_a for several representative values of the coupling g_{aWW} .

In general, displaced vertices can also be reconstructed in other detector components, such as the electromagnetic calorimeter (ECAL), hadronic calorimeter (HCAL) and the muon spectrometer (MS). In this work, we concentrate exclusively on the IT for the reconstruction of displaced vertices, as it provides precise vertex reconstruction for charged particles and is therefore

well suited for identifying displaced decays occurring close to the interaction point. A dedicated study of displaced vertex signals in the calorimeter systems would require specialized simulations and dedicated trigger strategies, which are beyond the scope of the present analysis. Compared to the IT, the MS is also not considered here, as its larger distance from the interaction point makes it more sensitive to particles with longer decay lengths and less sensitive to decays with relatively short lifetimes.

III. THE PROSPECTS FOR PROBING LIGHT PHOTOPHOBIC LONG-LIVED ALPS AT THE CEPC

In this section, we investigate the sensitivity of the 91.2 GeV CEPC to light long-lived photophobic ALPs via displaced vertex signals. Specifically, we consider the single-production processes of the photophobic ALP, $e^+e^- \rightarrow a\gamma$, $a\nu\bar{\nu}$, ae^+e^- and ajj . The Feynman diagrams for these processes and their corresponding production cross sections at the CEPC are presented in Figs. 3 and 4, respectively. As shown in Fig. 4, the photon-associated production process $e^+e^- \rightarrow a\gamma$ clearly dominates. For the ALPs with masses in the range of 1 – 10 GeV and $g_{aWW} = 1 \times 10^{-3} \text{ TeV}^{-1}$, its production cross sections vary from 1.746×10^{-5} to 1.683×10^{-5} pb, approximately three orders of magnitude larger than those of the other processes. For this process, the mediator can be either a photon or a Z boson. However, in the photophobic ALP scenario, the effective $a\gamma\gamma$ coupling is generated only at loop level. Consequently, the photon-mediated contribution accounts for only about 0.1% of the total production cross section and can be safely neglected. Then, the $a\gamma$ final state is predominantly produced via the on-shell decay $Z \rightarrow a\gamma$ at the Z pole of CEPC. We therefore focus on the production process $e^+e^- \rightarrow Z \rightarrow a\gamma$ and investigate the prospects for detecting ALP signals at the CEPC.

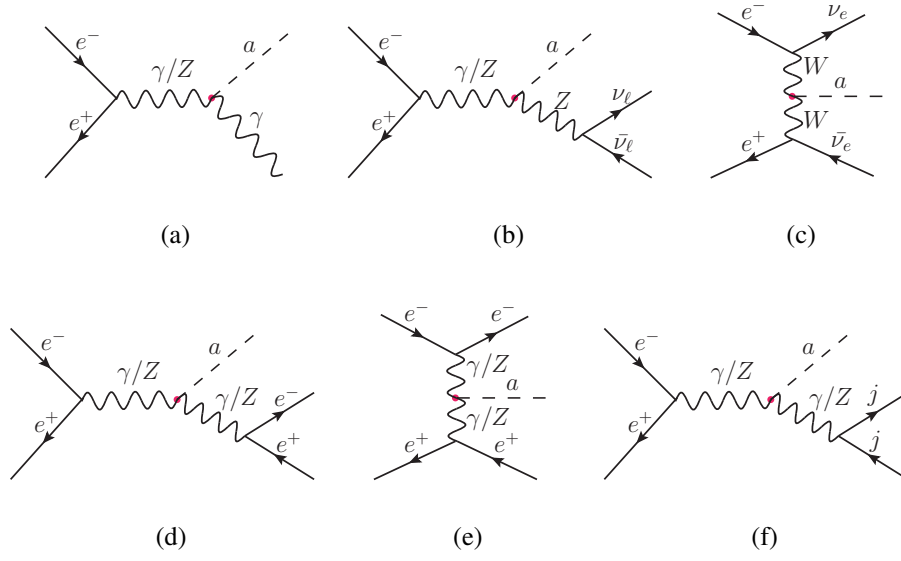


FIG. 3: The Feynman diagrams for the single-production processes of the photophobic ALP, $e^+e^- \rightarrow a\gamma$ (a), $a\nu\bar{\nu}$ (b,c), ae^+e^- (d,e) and ajj (f).

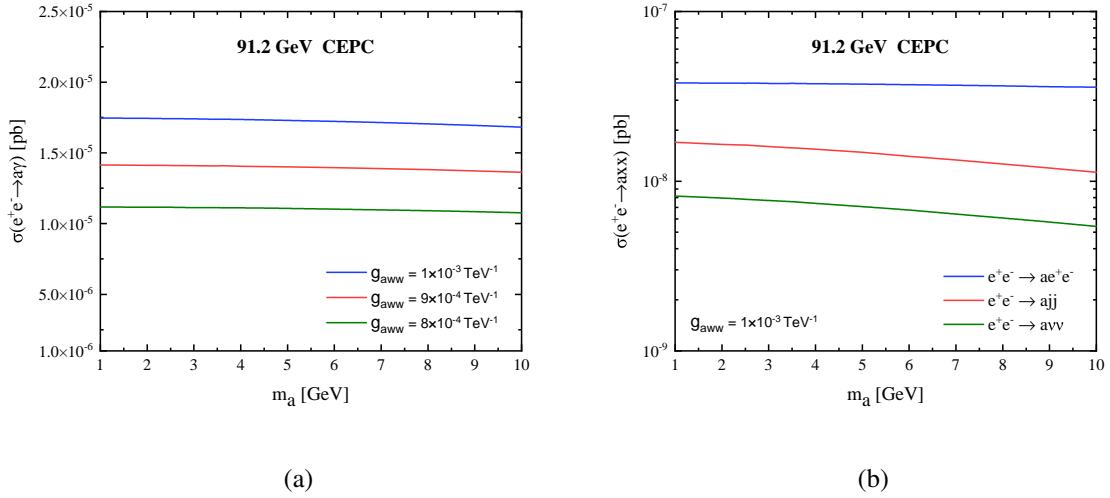


FIG. 4: The production cross sections of the processes $e^+e^- \rightarrow a\gamma$ (a), $a\nu\bar{\nu}$, ae^+e^- and ajj (b) as functions of the ALP mass m_a for different values of the coupling g_{aWW} at the 91.2 GeV CEPC.

We now focus on the production process $e^+e^- \rightarrow Z \rightarrow a\gamma$, where the ALP subsequently

decays into a pair of displaced charged leptons within the inner tracker detector of the CEPC with $\sqrt{s} = 91.2$ GeV and $\mathcal{L} = 100$ ab $^{-1}$. We consider the ALPs with masses in the range of 1 – 10 GeV, focusing on the displaced dimuon channel $a \rightarrow \mu^+\mu^-$ for $m_a = 1 - 4$ GeV and displaced ditau channel $a \rightarrow \tau^+\tau^-$ for $m_a = 4 - 10$ GeV. Since tau leptons are unstable, they can decay either leptonically or hadronically, with the hadronic modes having larger branching fractions. We therefore concentrate on the 1-prong hadronic tau decay modes as representative examples, where each τ decays via $\tau^\pm \rightarrow \pi^\pm\nu_\tau$ or $\tau^\pm \rightarrow \pi^\pm\pi^0\nu_\tau$. The corresponding signals are thus characterized by $\mu^+\mu^-\gamma$ for the dimuon channel and $\tau_h^+\tau_h^-\cancel{E}_T\gamma$ for the ditau channel.

For further calculation, we use `FeynRules` package [60] to generate the UFO model file for the effective Lagrangian. For the numerical results and the event generation, we choose the Monte Carlo (MC) simulation with the `MadGraph5_aMC@NLO` [61] to generate the signal and background events at parton level with the following basic cuts:

$$\begin{aligned}
\text{For the dimuon channel : } & p_T^\ell > 5 \text{ GeV}, \quad |\eta_\ell| < 2.5, \quad \text{with } \ell = \mu, \\
& p_T^\gamma > 10 \text{ GeV}, \quad |\eta_\gamma| < 2.5, \\
& \Delta R_{\ell\ell} > 0.4, \quad \Delta R_{\ell\gamma} > 0.4.
\end{aligned} \tag{10}$$

$$\text{For the ditau channel : } p_T^\gamma > 10 \text{ GeV}, \quad |\eta_\gamma| < 2.5.$$

Here, $\Delta R_{\ell\ell}$ and $\Delta R_{\ell\gamma}$ defined as $\sqrt{(\Delta\phi)^2 + (\Delta\eta)^2}$ refer to the angular separation between the two leptons and between the lepton and the photon, respectively. p_T^ℓ and p_T^γ are the transverse momenta of leptons and photons, $|\eta_\ell|$ and $|\eta_\gamma|$ are the absolute values of the pseudorapidity of leptons and photons. Then we use `PYTHIA8` program [62] to perform the parton showering. To simulate the detector effects, we use the simplified fast simulation (SFS) framework [63] embedded in `MadAnalysis5`. [64–66]. The subsequent kinematic and cut-based analysis are performed using C++ programming in the expert mode of `MadAnalysis5`.

A. The $\mu^+\mu^-\gamma$ signal

We now focus on the $\mu^+\mu^-\gamma$ signal for ALPs with masses in the range of 1 – 4 GeV. Its production cross sections at the CEPC are shown in Fig. 5. In general, the production cross section exhibits a decreasing trend as m_a increases. A noticeable suppression appears around $m_a \simeq 2.5$ GeV due to the kinematic opening of the $a \rightarrow c\bar{c}$ decay channel, which reduces

the branching ratio of $a \rightarrow \mu^+\mu^-$ and consequently suppresses the $\mu^+\mu^-\gamma$ signal. After applying the basic cuts described above, the values of the production cross sections range from 4.549×10^{-4} to 3.625×10^{-6} pb, 1.137×10^{-4} to 9.053×10^{-7} pb and 4.550×10^{-6} to 3.621×10^{-8} pb for $g_{aWW} = 1 \times 10^{-2}$ TeV $^{-1}$, 5×10^{-3} TeV $^{-1}$ and 1×10^{-3} TeV $^{-1}$, respectively. The dominant SM background in our numerical analysis originates from the process $e^+e^- \rightarrow \mu^+\mu^-\gamma$, with the production cross section of approximately 28.256 pb. In addition to this irreducible background, instrumental backgrounds such as pile-up interactions, vertices originating from dense detector regions and random-track crossings may in principle be present. A quantitative assessment of these effects requires dedicated detector-level simulations and specialized reconstruction techniques, which are beyond the scope of this study. Accordingly, the results presented in this paper are under the simplifying assumption that these instrumental backgrounds are negligible.

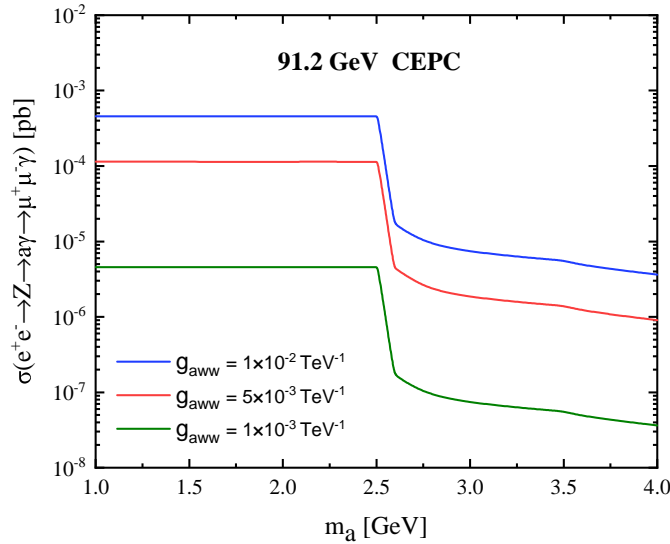


FIG. 5: The production cross sections of the $\mu^+\mu^-\gamma$ signal as functions of the ALP mass m_a for several representative values of the coupling g_{aWW} at the 91.2 GeV CEPC.

Several displacement observables are used to distinguish the signal from the SM background, including $|d_0^\mu|$, v_0^μ and v_z^μ . The observable $|d_0^\mu|$ denotes the transverse impact parameter of the charged muon, defined as the distance of closest approach between the helical trajectory of the muon track and the beam axis in the transverse plane. The observables v_0^μ and v_z^μ correspond

to the transverse and longitudinal distances of the muon production vertex with respect to the interaction point. In addition to these displacement observables, we also consider the angular separation $\Delta R_{\mu^+\mu^-}$ and the transverse momentum $P_T^{\mu^+\mu^-}$ of the reconstructed ALP to further pick out the signal from the SM background. The normalized distributions of these observables for the $\mu^+\mu^-\gamma$ signal with the ALP mass $m_a = 1, 2, 3$ and 4 GeV and the fixed coupling $g_{aWW} = 5 \times 10^{-3} \text{ TeV}^{-1}$ as well as the SM background at the 91.2 GeV CEPC with $\mathcal{L} = 100 \text{ ab}^{-1}$ are shown in Fig. 6.

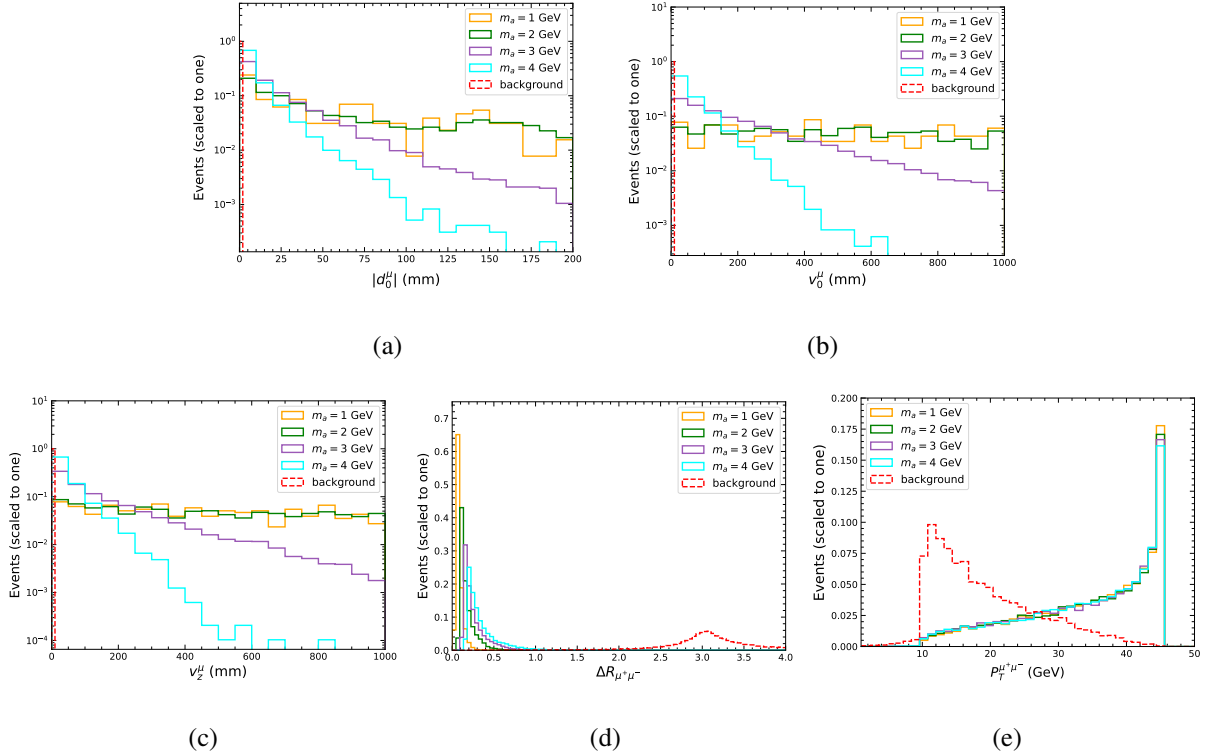


FIG. 6: The normalized distributions of $|d_0^\mu|$, v_0^μ , v_z^μ , $\Delta R_{\mu^+\mu^-}$ and $P_T^{\mu^+\mu^-}$ for the $\mu^+\mu^-\gamma$ signal with selected ALP mass benchmark points and $g_{aWW} = 5 \times 10^{-3} \text{ TeV}^{-1}$ as well as the SM background at the 91.2 GeV CEPC with $\mathcal{L} = 100 \text{ ab}^{-1}$.

From Fig. 6(a-c), it can be seen that the signal events exhibit broad distributions with extended tails in $|d_0^\mu|$, v_0^μ and v_z^μ , reflecting the displaced decay of a light long-lived ALP. In contrast, the background events mainly originate from promptly decaying particles and therefore concentrated at small values of these observables. As shown in Fig. 6(d), the two charged muons from a light ALP decay tend to be collimated, whereas their angular separation in the

background events exhibits a much broader distribution. Figure 6(e) shows the $P_T^{\mu^+\mu^-}$ distribution. For the signal events, the ALP is produced via the two-body decay $Z \rightarrow \gamma a$ and is therefore typically highly boosted, leading to a dimuon system with relatively large transverse momentum. By contrast, the dimuon pair from the background events generally carries smaller transverse momentum, leading to a distribution concentrated in the low- P_T region.

Based on the characteristic features of these distributions, the optimized cuts for the identification of the $\mu^+\mu^-\gamma$ signal and suppression of the SM background are summarized in Table I with the number cuts being taken as the first step filter. These cuts include fiducial requirements on the displacement observables: $|d_0^\mu| > 2$ mm, $0.1 \text{ m} < v_0^\mu < 1.8 \text{ m}$ and $v_z^\mu < 2.35 \text{ m}$, chosen according to the detector geometry and previous displaced vertex studies [29, 34, 37], ensuring that the ALP decays occur inside the sensitive region of the inner tracker detector. After applying all optimized cuts, the SM background is expected to be suppressed to a negligible level. In Table II, we summarize the cumulative selection efficiency ϵ and production cross section σ of the $\mu^+\mu^-\gamma$ signal for representative ALP mass points with $g_{aWW} = 5 \times 10^{-3} \text{ TeV}^{-1}$ after the step-by-step optimized cuts employed at the 91.2 GeV CEPC with $\mathcal{L} = 100 \text{ ab}^{-1}$. The cumulative selection efficiency can range from 8.00×10^{-3} to 1.63×10^{-1} for ALP masses between 1 and 4 GeV.

TABLE I: The optimized cuts on the $\mu^+\mu^-\gamma$ signal and SM background for $1 \text{ GeV} \leq m_a \leq 4 \text{ GeV}$ at the 91.2 GeV CEPC with $\mathcal{L} = 100 \text{ ab}^{-1}$.

Optimized cuts	Selection criteria
Cut 1: the multiplicity of the muon in the final states	$N_{\mu^+} \geq 1, N_{\mu^-} \geq 1$
Cut 2: the transverse impact parameter	$ d_0^\mu > 2 \text{ mm}$
Cut 3: the transverse and longitudinal distance	$0.1 \text{ m} < v_0^\mu < 1.8 \text{ m}, v_z^\mu < 2.35 \text{ m}$
Cut 4: the angular separation between the two charged muons	$\Delta R_{\mu^+\mu^-} < 1.0$
Cut 5: the transverse momentum of reconstructed ALP	$p_T^{\mu^+\mu^-} > 25 \text{ GeV}$

TABLE II: The cumulative selection efficiency ϵ and production cross section σ of the $\mu^+\mu^-\gamma$ signal for representative ALP mass points with $g_{aWW} = 5 \times 10^{-3} \text{ TeV}^{-1}$ after the step-by-step optimized cuts employed at the 91.2 GeV CEPC with $\mathcal{L} = 100 \text{ ab}^{-1}$.

Cuts	Cross sections [pb] (selection efficiencies) for the signal			
	$m_a = 1 \text{ GeV}$	$m_a = 2 \text{ GeV}$	$m_a = 3 \text{ GeV}$	$m_a = 4 \text{ GeV}$
Generator:	1.137×10^{-4}	1.138×10^{-4}	1.813×10^{-6}	9.053×10^{-7}
Cut 1:	1.064×10^{-4} (9.36×10^{-1})	1.050×10^{-4} (9.22×10^{-1})	1.667×10^{-6} (9.20×10^{-1})	8.318×10^{-7} (9.19×10^{-1})
Cut 2:	1.063×10^{-4} (9.34×10^{-1})	1.042×10^{-4} (9.15×10^{-1})	1.096×10^{-6} (6.05×10^{-1})	3.457×10^{-7} (3.82×10^{-1})
Cut 3:	1.135×10^{-6} (1.00×10^{-2})	5.462×10^{-6} (4.80×10^{-2})	9.027×10^{-7} (4.98×10^{-1})	1.574×10^{-7} (1.74×10^{-1})
Cut 4:	1.135×10^{-6} (1.00×10^{-2})	5.462×10^{-6} (4.80×10^{-2})	9.027×10^{-7} (4.98×10^{-1})	1.574×10^{-7} (1.74×10^{-1})
Cut 5:	9.091×10^{-7} (8.00×10^{-3})	3.411×10^{-6} (3.00×10^{-2})	7.611×10^{-7} (4.20×10^{-1})	1.474×10^{-7} (1.63×10^{-1})

The number of signal events passing the optimized selection criteria is given by $N_{sig} = \epsilon \times \sigma \times \mathcal{L}$. After applying these criteria, the SM background is found to be negligible in our analysis. Therefore, we take 3 signal events as the benchmark for the 95% confidence level (C.L.) exclusion limit. The projected 95% C.L. sensitivity of the 91.2 GeV CEPC with $\mathcal{L} = 100 \text{ ab}^{-1}$ to light long-lived photophobic ALPs via the $\mu^+\mu^-\gamma$ signal is shown by the purple area of Fig. 9.

B. The $\tau_h^+\tau_h^-\cancel{E}_T\gamma$ signal

In this subsection, we investigate the signal from the process $e^+e^- \rightarrow Z \rightarrow a\gamma \rightarrow \tau^+\tau^-\gamma$, focusing on subsequent hadronic tau decays. Each hadronic tau decay is reconstructed as a narrow tau jet containing a single charged track, so the signal is characterized by two oppositely charged tau jets, missing transverse energy and a photon, denoted as $\tau_h^+\tau_h^-\cancel{E}_T\gamma$. The corresponding production cross sections at the CEPC as functions of the ALP mass m_a for different values of g_{aWW} are shown in Fig. 7. For m_a in the range of 4 – 10 GeV, the values of the production cross sections range from 5.320×10^{-5} to 1.835×10^{-5} pb, 1.330×10^{-5} to 4.589×10^{-6} pb and 5.320×10^{-7} to 1.835×10^{-7} pb for $g_{aWW} = 1 \times 10^{-2}$, 5×10^{-3} and $1 \times 10^{-3} \text{ TeV}^{-1}$, respectively. These results are obtained after applying the basic cuts described above. The dominant SM background in our numerical analysis arises from the process $e^+e^- \rightarrow \tau^+\tau^-\gamma$, with both taus decaying via the 1-prong hadronic mode. The corresponding production cross section

is approximately 4.975 pb.

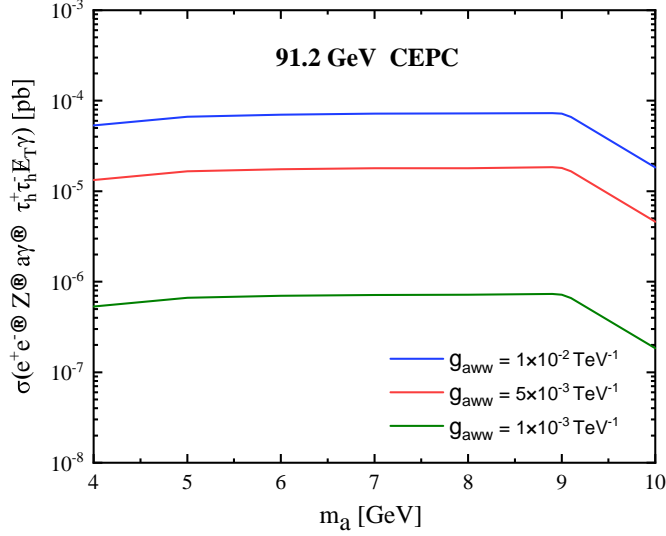


FIG. 7: Same as Fig. 5 but for the $\tau_h^+ \tau_h^- \cancel{E}_T \gamma$ signal.

To effectively separate the signal from the SM background, we consider several observables similar to those used in the $\mu^+ \mu^- \gamma$ signal analysis, including $|d_0^{\tau_h}|$, $v_0^{\tau_h}$, $v_z^{\tau_h}$, $\Delta R_{\tau_h^+ \tau_h^-}$ and $P_T^{\tau_h^+ \tau_h^-}$. Their normalized distributions for the $\tau_h^+ \tau_h^- \cancel{E}_T \gamma$ signal and the corresponding SM background at the 91.2 GeV CEPC with $\mathcal{L} = 100 \text{ ab}^{-1}$ are shown in Fig. 8. As illustrated in this figure, the signal and background events can be clearly distinguished using these observables. Based on the features of these distributions, we apply optimized cuts similar to those employed in the $\mu^+ \mu^- \gamma$ signal analysis, but require $P_T^{\tau_h^+ \tau_h^-} > 30 \text{ GeV}$. After applying these optimized cuts, the SM background is reduced to a level that can be considered negligible. Table III summarizes the cumulative selection efficiency ϵ and production cross section σ for the $\tau_h^+ \tau_h^- \cancel{E}_T \gamma$ signal at the 91.2 GeV CEPC with $\mathcal{L} = 100 \text{ ab}^{-1}$, with ϵ ranging from 8.30×10^{-2} to 7.60×10^{-2} for $m_a = 5 - 8 \text{ GeV}$.

With negligible SM background, we take $N_{sig} = 3$ to obtain the expected 95% C.L. sensitivity of the 91.2 GeV CEPC with $\mathcal{L} = 100 \text{ ab}^{-1}$ to light long-lived ALPs via the $\tau_h^+ \tau_h^- \cancel{E}_T \gamma$ signal, as indicated by the pink region in Fig. 9. In this figure, we only display the parameter space for $m_a = 4 - 9 \text{ GeV}$. For ALP masses above the $b\bar{b}$ threshold, its total decay width increases significantly, leading to a much shorter lifetime. As a result, the ALP decays become

too prompt to satisfy the displaced decay requirements within the inner tracker detector, leaving no accessible parameter space for the long-lived ALPs in this mass region.

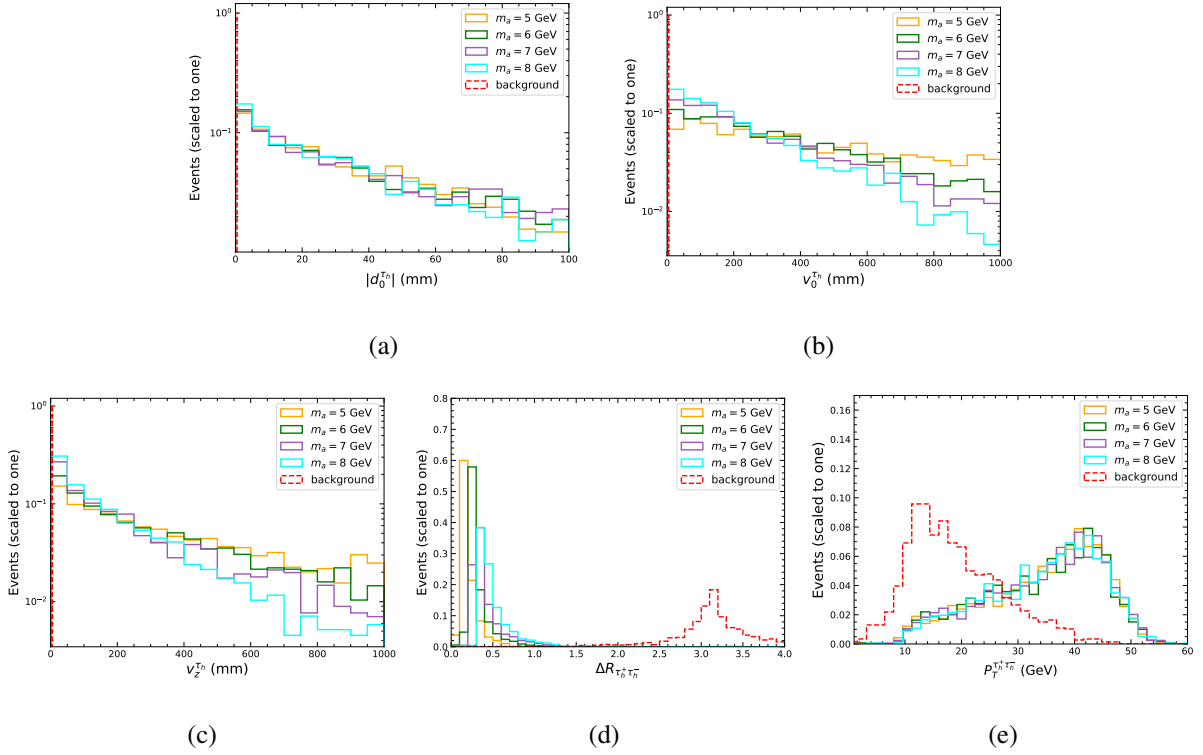


FIG. 8: Same as Fig. 6 but for the observables $|d_0^{T_h}|$, $v_0^{T_h}$, $v_z^{T_h}$, $\Delta R_{\tau_h^+ \tau_h^-}$ and $P_T^{\tau_h^+ \tau_h^-}$ with $g_{aWW} = 1 \times 10^{-3} \text{ TeV}^{-1}$.

TABLE III: Same as Table II but for the $\tau_h^+ \tau_h^- \cancel{E}_T \gamma$ signal with $g_{aWW} = 1 \times 10^{-3} \text{ TeV}^{-1}$.

Cuts	Cross sections [pb] (efficiencies) for the signal			
	$m_a = 5 \text{ GeV}$	$m_a = 6 \text{ GeV}$	$m_a = 7 \text{ GeV}$	$m_a = 8 \text{ GeV}$
Generator:	6.653×10^{-7}	6.998×10^{-7}	7.145×10^{-7}	7.187×10^{-7}
Cut 1:	1.084×10^{-7} (1.63×10^{-1})	1.112×10^{-7} (1.59×10^{-1})	1.129×10^{-7} (1.58×10^{-1})	1.130×10^{-7} (1.57×10^{-1})
Cut 2:	9.778×10^{-8} (1.47×10^{-1})	9.721×10^{-8} (1.39×10^{-1})	9.646×10^{-8} (1.35×10^{-1})	9.271×10^{-8} (1.29×10^{-1})
Cut 3:	8.316×10^{-8} (1.13×10^{-1})	8.258×10^{-8} (1.18×10^{-1})	7.931×10^{-8} (1.11×10^{-1})	7.331×10^{-8} (1.02×10^{-1})
Cut 4:	8.316×10^{-8} (1.13×10^{-1})	8.258×10^{-8} (1.18×10^{-1})	7.931×10^{-8} (1.11×10^{-1})	7.115×10^{-8} (9.90×10^{-2})
Cut 5:	5.522×10^{-8} (8.30×10^{-2})	5.738×10^{-8} (8.20×10^{-2})	5.716×10^{-8} (8.00×10^{-2})	5.462×10^{-8} (7.60×10^{-2})

In Fig. 9, we present the projected 95% C.L. sensitivities of the 91.2 GeV CEPC with

$\mathcal{L} = 100 \text{ ab}^{-1}$ to light long-lived photophobic ALPs. The purple and pink shaded regions denote the projected sensitivities obtained from the $\mu^+\mu^-\gamma$ and $\tau_h^+\tau_h^-\cancel{E}_T\gamma$ signals, respectively. For the $\mu^+\mu^-\gamma$ signal, the CEPC is expected to probe the coupling in the range $g_{aWW} \in [1.27 \times 10^{-3}, 6.80 \times 10^{-1}] \text{ TeV}^{-1}$ for $m_a \in [1, 4] \text{ GeV}$. While for the $\tau_h^+\tau_h^-\cancel{E}_T\gamma$ signal, the prospective sensitivities of the CEPC can reach $g_{aWW} \in [7.00 \times 10^{-4}, 9.40 \times 10^{-3}] \text{ TeV}^{-1}$ for $m_a \in [4, 9] \text{ GeV}$. Other excluded regions for photophobic ALPs from previous studies for $1 \text{ GeV} \leq m_a \leq 100 \text{ GeV}$ are also shown in the colored shaded regions of the Fig. 9. The gray and dark-gray regions represent the constraints on long-lived ALPs obtained by the LHCb collaboration via the processes $B^0 \rightarrow K^{0*}a$ and $B^\pm \rightarrow K^\pm a$ with $a \rightarrow \mu^+\mu^-$ [67, 68]. The cyan region marked ‘‘Charm’’ corresponds to the bounds on long-lived ALPs obtained from the CHARM experiment [69]. The yellow region marked ‘‘LEP’’ denotes the constraints derived from the decays $Z \rightarrow \gamma a \rightarrow \gamma\gamma\cancel{E}_T$ and $Z \rightarrow \gamma a \rightarrow \gamma jj$ at the Z pole of the LEP [70, 71]. The green region marked ‘‘LHC’’ indicates the exclusion limits from various searches at the LHC [49], while the red region shows the bounds obtained from a dedicated Run-II 13 TeV LHC analysis targeting the process $pp \rightarrow a jj \rightarrow Z(\rightarrow \nu\bar{\nu})\gamma jj$ [50]. Finally, the orange and blue regions indicate the projected sensitivities of the HL-LHC to light long-lived ALP via the process $pp \rightarrow \gamma a \rightarrow \gamma\tau^+\tau^-$, with the tau leptons decaying either hadronically or leptonically, respectively [72].

Comparing our results with the regions excluded by other experiments, we find that the 91.2 GeV CEPC with $\mathcal{L} = 100 \text{ ab}^{-1}$ can probe long-lived photophobic ALPs with lighter masses and weaker couplings via the $\mu^+\mu^-\gamma$ and $\tau_h^+\tau_h^-\cancel{E}_T\gamma$ signals, accessing parameter regions that are beyond the reach of prompt decay searches at the LEP and LHC. In addition, compared with the constraints on long-lived ALPs from rare meson decays obtained by the LHCb collaboration and the CHARM experiment, the CEPC can provide complementary coverage of the light long-lived ALP parameter space. Furthermore, the projected sensitivity obtained in this work is also complementary to the expected reach of the HL-LHC. In summary, these results indicate that the 91.2 GeV CEPC with $\mathcal{L} = 100 \text{ ab}^{-1}$ exhibits strong potential to explore light long-lived photophobic ALPs through displaced vertex signals within the inner tracker detector.

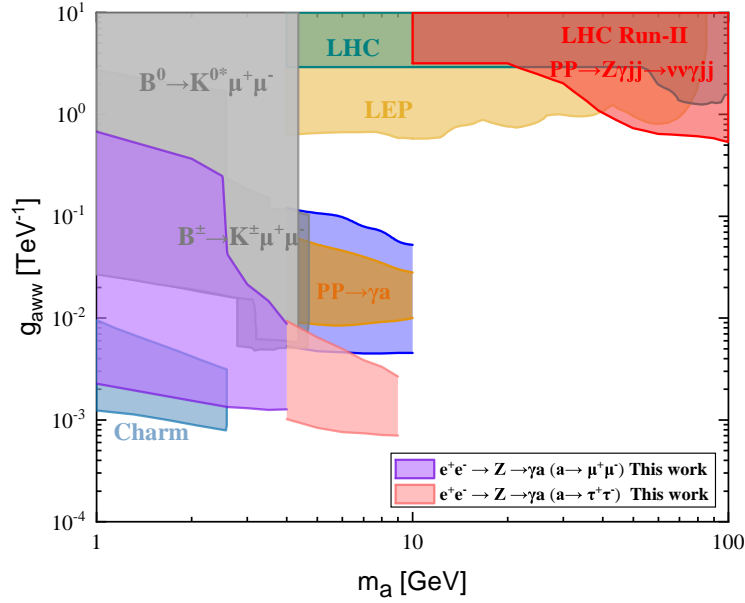


FIG. 9: Our projected 95% C.L. sensitivities of the CEPC to light long-lived photophobic ALPs via the $\mu^+\mu^-\gamma$ (purple region) and $\tau_h^+\tau_h^-\cancel{E}_T\gamma$ (pink region) signals in comparison with other excluded regions.

IV. CONCLUSIONS AND DISCUSSIONS

So far, a wide variety of new physics models have been proposed to solve open problems of the SM and potential experimental anomalies, many of which predict the presence of new particles. Searching for the possible signals of these new particles is one of the primary goals of current and future collider experiments. As a well-motivated class of new particles, ALPs can give rise to rich phenomenology in both low- and high-energy experiments and therefore merit extensive study. Many previous studies have focused on probing ALPs via their prompt-decay or the associated missing-energy signals.

In this paper, we have investigated the prospects for detecting light long-lived photophobic ALPs through displaced vertex signals within the inner tracker detector of the CEPC with $\sqrt{s} = 91.2$ GeV and $\mathcal{L} = 100$ ab^{-1} . We consider the production of a photophobic ALP in association with a photon, a lepton pair or a jet pair. Among these production processes, we find that the

photon-associated production mode exhibits the largest production cross section. We therefore focus on the process $e^+e^- \rightarrow Z \rightarrow \gamma a$, with the ALP a subsequently decaying into a pair of displaced muon and tau leptons. We perform Monte Carlo simulations for the $\mu^+\mu^-\gamma$ and $\tau_h^+\tau_h^-\cancel{E}_T\gamma$ signals and derive prospective 95% C.L. sensitivities of the CEPC to light long-lived photophobic ALPs. For the $\mu^+\mu^-\gamma$ signal, the CEPC can probe the ALP- W boson coupling in the range $g_{aWW} \in [1.27 \times 10^{-3}, 6.80 \times 10^{-1}] \text{ TeV}^{-1}$ for $m_a \in [1, 4] \text{ GeV}$. While for the $\tau_h^+\tau_h^-\cancel{E}_T\gamma$ signal, the prospective sensitivities reach $g_{aWW} \in [7.00 \times 10^{-4}, 9.40 \times 10^{-3}] \text{ TeV}^{-1}$ for $m_a \in [4, 9] \text{ GeV}$. Comparing our results with exclusion regions from other experiments, we find that the CEPC can probe regions of the photophobic ALP parameter space characterized by lower masses and weaker couplings that remain challenging for prompt-decay searches at the LEP and LHC. In addition, compared with the constraints from rare meson decays obtained by the LHCb collaboration and the CHARM experiment, the CEPC can provide complementary coverage of the light long-lived ALP parameter space. Furthermore, the projected sensitivity obtained in this work is also complementary to the expected reach of the HL-LHC. Thus, we can conclude that the CEPC has great potential to detect light long-lived photophobic ALPs via displaced vertex signals.

In this paper, we primarily explore the potential of the CEPC for detecting light long-lived ALPs, taking advantage of its clean experimental environment, high integrated luminosity and precise measurement capabilities. Other future lepton colliders, such as the FCC-ee, are also expected to offer promising opportunities for probing light long-lived ALPs. However, their center-of-mass energy, integrated luminosity and detailed detector design differ from those of the CEPC and therefore require dedicated analyses. In this study, we take the CEPC simply as a representative example and expect that our results may provide valuable insights for detecting light long-lived ALPs at the FCC-ee.

ACKNOWLEDGMENT

This work was partially supported by the National Natural Science Foundation of China under Grant No. 12575106 and the Cultivation Fund of Liaoning Normal University for Excellent

- [1] M. C. Gonzalez-Garcia and M. Maltoni, Phys. Rept. **460**, 1 (2008), 0704.1800.
- [2] G. Bertone, D. Hooper, and J. Silk, Phys. Rept. **405**, 279 (2005), hep-ph/0404175.
- [3] K. R. Dienes and B. Thomas, Phys. Rev. D **85**, 083523 (2012), 1106.4546.
- [4] R. D. Peccei and H. R. Quinn, Phys. Rev. Lett. **38**, 1440 (1977).
- [5] R. D. Peccei and H. R. Quinn, Phys. Rev. D **16**, 1791 (1977).
- [6] F. Wilczek, Phys. Rev. Lett. **40**, 279 (1978).
- [7] J. L. Feng, Ann. Rev. Nucl. Part. Sci. **63**, 351 (2013), 1302.6587.
- [8] G. Lanfranchi, M. Pospelov, and P. Schuster, Ann. Rev. Nucl. Part. Sci. **71**, 279 (2021), 2011.02157.
- [9] C. Antel et al., Eur. Phys. J. C **83**, 1122 (2023), 2305.01715.
- [10] L. Jeanty and B. Shuve (2025), 2511.17934.
- [11] M. Aaboud et al. (ATLAS), Phys. Rev. D **99**, 012001 (2019), 1808.03057.
- [12] G. Aad et al. (ATLAS), Phys. Lett. B **801**, 135114 (2020), 1907.10037.
- [13] G. Aad et al. (ATLAS), JHEP **06**, 200 (2023), 2301.13866.
- [14] G. Aad et al. (ATLAS), Phys. Rev. D **102**, 032006 (2020), 2003.11956.
- [15] G. Aad et al. (ATLAS), Eur. Phys. J. C **80**, 450 (2020), 1909.01246.
- [16] M. Aaboud et al. (ATLAS), Phys. Rev. D **99**, 052005 (2019), 1811.07370.
- [17] G. Aad et al. (ATLAS), Phys. Rev. D **101**, 052013 (2020), 1911.12575.
- [18] G. Aad et al. (ATLAS), Phys. Rev. D **106**, 032005 (2022), 2203.00587.
- [19] G. Aad et al. (ATLAS), JHEP **06**, 005 (2022), 2203.01009.
- [20] G. Aad et al. (ATLAS), JHEP **11**, 229 (2021), 2107.06092.
- [21] M. Aaboud et al. (ATLAS), JHEP **10**, 031 (2018), 1806.07355.
- [22] A. Tumasyan et al. (CMS), JHEP **05**, 228 (2023), 2205.08582.
- [23] A. Tumasyan et al. (CMS), JHEP **04**, 062 (2022), 2112.13769.
- [24] A. M. Sirunyan et al. (CMS), Phys. Rev. D **104**, 052011 (2021), 2104.13474.
- [25] A. M. Sirunyan et al. (CMS), Phys. Rev. D **104**, 012015 (2021), 2012.01581.
- [26] A. Tumasyan et al. (CMS), JHEP **03**, 160 (2022), 2110.13218.
- [27] R. Aaij et al. (LHCb), Eur. Phys. J. C **77**, 812 (2017), 1705.07332.

- [28] R. Aaij et al. (LHCb), *Eur. Phys. J. C* **76**, 664 (2016), 1609.03124.
- [29] M. Dong et al. (CEPC Study Group) (2018), 1811.10545.
- [30] W. Abdallah et al. (CEPC Study Group), *Radiat. Detect. Technol. Methods* **8**, 1 (2024), [Erratum: *Radiat. Detect. Technol. Methods* **9**, 184–192 (2025)], 2312.14363.
- [31] A. Abada et al. (FCC), *Eur. Phys. J. ST* **228**, 261 (2019).
- [32] M. Benedikt et al. (FCC), *Eur. Phys. J. C* **85**, 1468 (2025), 2505.00272.
- [33] J. Gao (CEPC Accelerator Study Group) (2022), 2203.09451.
- [34] K. Cheung and Z. S. Wang, *Phys. Rev. D* **101**, 035003 (2020), 1911.08721.
- [35] Z. S. Wang and K. Wang, *Phys. Rev. D* **101**, 115018 (2020), 1904.10661.
- [36] S. Alipour-Fard, N. Craig, M. Jiang, and S. Koren, *Chin. Phys. C* **43**, 053101 (2019), 1812.05588.
- [37] Q.-H. Cao, J. Guo, J. Liu, Y. Luo, and X.-P. Wang, *Phys. Rev. D* **110**, 015029 (2024), 2311.12934.
- [38] R. G. Suarez, *Acta Phys. Polon. B* **52**, 953 (2021), 2102.07597.
- [39] Y. Zhang, C. Mo, X. Chen, B. Li, H. Chen, J. Hu, and L. Li, *Front. Phys. (Beijing)* **21**, 056202 (2026), 2401.05094.
- [40] A. Blondel et al., *Front. in Phys.* **10**, 967881 (2022), 2203.05502.
- [41] K. A. Urquía-Calderón, *Phys. Rev. D* **109**, 055002 (2024), 2310.17406.
- [42] M. Chruszcz, R. G. Suarez, and S. Monteil, *Eur. Phys. J. Plus* **136**, 1056 (2021), 2106.15459.
- [43] J. E. Kim, *Phys. Rev. Lett.* **43**, 103 (1979).
- [44] M. A. Shifman, A. I. Vainshtein, and V. I. Zakharov, *Nucl. Phys. B* **166**, 493 (1980).
- [45] M. Dine, W. Fischler, and M. Srednicki, *Phys. Lett. B* **104**, 199 (1981).
- [46] A. R. Zhitnitsky, *Sov. J. Nucl. Phys.* **31**, 260 (1980).
- [47] A. A. Anselm and N. G. Uraltsev, *Phys. Lett. B* **114**, 39 (1982).
- [48] A. Ringwald, in *49th Rencontres de Moriond on Electroweak Interactions and Unified Theories* (2014), pp. 223–230, 1407.0546.
- [49] N. Craig, A. Hook, and S. Kasko, *JHEP* **09**, 028 (2018), 1805.06538.
- [50] M. Aiko, M. Endo, and K. Fridell, *JHEP* **06**, 194 (2024), 2401.13323.
- [51] Z. Ding, Y.-n. Mao, and K. Wang, *JHEP* **06**, 087 (2025), 2411.08660.
- [52] Y.-n. Mao, K. Wang, and Y. Xiong, *Chin. Phys. C* **49**, 083106 (2025), 2411.14041.
- [53] J. Feng, Y.-n. Mao, and K. Wang (2025), 2511.21003.
- [54] Z. Ding, J. Feng, Y.-n. Mao, K. Wang, and Y. Xiong (2025), 2512.23155.

- [55] S.-Y. Wang, Y.-P. Jiao, H.-H. Zhang, and G. Cacciapaglia (2025), 2509.17718.
- [56] H. Georgi, D. B. Kaplan, and L. Randall, *Phys. Lett. B* **169**, 73 (1986).
- [57] M. Bauer, M. Neubert, and A. Thamm, *JHEP* **12**, 044 (2017), 1708.00443.
- [58] M. Bauer, M. Neubert, S. Renner, M. Schnubel, and A. Thamm, *JHEP* **04**, 063 (2021), 2012.12272.
- [59] J. Bonilla, I. Brivio, M. B. Gavela, and V. Sanz, *JHEP* **11**, 168 (2021), 2107.11392.
- [60] A. Alloul, N. D. Christensen, C. Degrande, C. Duhr, and B. Fuks, *Comput. Phys. Commun.* **185**, 2250 (2014), 1310.1921.
- [61] J. Alwall, R. Frederix, S. Frixione, V. Hirschi, F. Maltoni, O. Mattelaer, H. S. Shao, T. Stelzer, P. Torrielli, and M. Zaro, *JHEP* **07**, 079 (2014), 1405.0301.
- [62] T. Sjöstrand, S. Ask, J. R. Christiansen, R. Corke, N. Desai, P. Ilten, S. Mrenna, S. Prestel, C. O. Rasmussen, and P. Z. Skands, *Comput. Phys. Commun.* **191**, 159 (2015), 1410.3012.
- [63] J. Y. Araz, B. Fuks, and G. Polykratis, *Eur. Phys. J. C* **81**, 329 (2021), 2006.09387.
- [64] E. Conte, B. Fuks, and G. Serret, *Comput. Phys. Commun.* **184**, 222 (2013), 1206.1599.
- [65] E. Conte, B. Dumont, B. Fuks, and C. Wymant, *Eur. Phys. J. C* **74**, 3103 (2014), 1405.3982.
- [66] E. Conte and B. Fuks, *Int. J. Mod. Phys. A* **33**, 1830027 (2018), 1808.00480.
- [67] R. Aaij et al. (LHCb), *Phys. Rev. D* **95**, 071101 (2017), 1612.07818.
- [68] R. Aaij et al. (LHCb), *Phys. Rev. Lett.* **115**, 161802 (2015), 1508.04094.
- [69] F. Bergsma et al. (CHARM), *Phys. Lett. B* **157**, 458 (1985).
- [70] P. D. Acton et al. (OPAL), *Phys. Lett. B* **311**, 391 (1993).
- [71] O. Adriani et al. (L3), *Phys. Lett. B* **292**, 472 (1992).
- [72] C.-X. Yue, X.-Y. Li, S. Yang, and M.-S.-Y. Wang, *Eur. Phys. J. C* **85**, 1442 (2025), 2510.24097.